Structure and properties of surface and subsurface defects in graphite accounting for van der Waals and spin-polarization effects

G. Teobaldi,[1,2,*] K. Tanimura,[1] and A. L. Shluger[2,3]
[1]*The Institute of Scientific and Industrial Research (ISIR), Osaka University, Mihogaoka 8-1, Ibaraki, Osaka 567-0047, Japan*
[2]*Department of Physics and Astronomy, University College London, Gower Street, WC1E 6BT London, United Kingdom*
[3]*WPI-AIMR, Tohoku University, 2-1-1 Kitahira, Aoba, Sendai 980-8577, Japan*
(Received 25 September 2010; published 4 November 2010)

The geometries, formation energies, and diffusion barriers of surface and subsurface intrinsic defects in graphite are calculated using spin-polarized density-functional theory and the generalized gradient approximation with a semiempirical van der Waals (vdW) correction for dispersion interactions. The calculated formation energies and diffusion barriers of subsurface interstitial (I) atoms deviate qualitatively and quantitatively from those of surface adatoms. The same trend is found also for subsurface and adatom clusters (I_2,I_3). In spite of the semiquantitative agreement on the optimized geometries, the formation energies and diffusion barriers of surface and subsurface vacancies (V), divacancies (VV), and intimate (I-V) Frenkel pairs differ significantly from the values for the analogous defects in the bulk of graphite. This suggests limited transferability of the bulk and subsurface defect models to the surface of graphite. These findings are rationalized in terms of the balance between the covalent and vdW interaction terms at the surface, subsurface, and bulk of graphite. Finally, pairing of individual defects (adatoms, I and V) is calculated to be energetically advantageous both on the surface and in the subsurface regions. This process is shown to either saturate residual dangling bonds or produce singlet spin states, thus contributing to the quenching of residual spin polarization from damaged graphite surfaces.

DOI: 10.1103/PhysRevB.82.174104 PACS number(s): 68.35.Dv, 61.80.Az, 71.15.Mb, 81.05.uf

I. INTRODUCTION

Defects in graphite, graphene, and related nanostructures are known to alter the chemical and physical properties of these materials.[1,2] In particular, radiation damage of graphite has been long representing a major concern for nuclear industry.[3] The introduction of defects in carbon-based materials is also recognized as a versatile tool for tailoring their properties to technologically relevant functions.[4] Controlled introduction of defects in carbon-based nanostructures may allow one to tune the properties of carbon-based materials, and could potentially lead to applications in nanoelectronics,[5] spintronics,[6] portable magnetic devices,[4] and catalysis.[7,8]

These perceived advantages have stimulated the pursuit of viable routes to nanoengineer graphite-based systems via electron irradiation,[9] ion bombardment,[10–14] plasma oxidation,[15,16] and intense femtosecond (fs)-laser[17–20] pulses. The ensuing explosion of experimental information has further motivated first-principles studies of intrinsic defects in carbon-based nanostructures. Atomic-scale understanding of the structure, energy, and properties of intrinsic defects in graphite, graphene, and related structures is essential to assist and direct the design and optimization of new materials with technologically relevant applications.[4,21]

The experimental information on the structure, formation energies, and diffusion of intrinsic defects in the bulk of graphite stems mostly from indirect and sample-averaged experiments.[22–27] However, surface probing techniques capable of atomic resolution make studying surface defects relatively easier. Using scanning tunneling microscopy,[12–16] scanning tunneling spectroscopy,[17,28] atomic force microscopy,[15,29] electrostatic force microscopy,[30] magnetic forces microscopy,[10,11,31] and transmission electron microscopy[9,32] one can visualize both the formation and evolution of defects populations on the surface of graphite[10–13,15,16,29–31] and related nanostructures.[9] As a result, the generation of single vacancies (V),[13,16,21,28,33–39] multivacancies,[16,21] interstitials (I),[21,33,35,36,40,41] interstitial-vacancy pairs,[21,35,42] and more complicated structures[10,11,13,17,43,44] has been proposed on the basis of both experimental data and theoretical models. However, with just one exception,[40] all the available models stem from simulations of intrinsic defects in either single-layer graphene[34,37] or bulk graphite.[21,35,36,38,39,41–44] To the best of our knowledge, there have not been any first-principles calculations of the structure and properties of intrinsic defects at the surface of graphite, with the only exception of the results for isolated interstitials on bilayer graphene.[40]

With the only exception of Refs. 40 and 44, the currently available atomic-scale models of defects in bulk graphite and single-layer graphene originate from local-density approximation (LDA)[21,34,42,43] or semilocal generalized gradient approximation (GGA)[35–39,41] density-functional theory (DFT) calculations, which do not account for the long-range van der Waals (vdW) interactions.[45–47] This deficiency is responsible for the tendency of LDA to favor diamond with respect to graphite as the most stable carbon phase[44,48,49] and for the poor performance of GGA in predicting the interlayer distance in graphite.[44,48–53] It has recently been demonstrated that inclusion of the vdW interactions in the simulations provides the experimental interlayer distance, which profoundly affects the energy and properties of intrinsic defects in the bulk of graphite.[44] In this paper we extend this work further and present the results of a comprehensive investigation of intrinsic defects and their aggregates at the surface of graph-

ite taking into account the vdW interactions. This allows us to reveal substantial differences in the relative stability and properties of the surface and subsurface defects. Finally, by comparison with previous bulk results, we also address the transferability of bulk-defect models to the surface of graphite.

Although recent implementations of ab inito vdW functionals are becoming increasingly accurate and efficient,[45–47] we opted for semiempirical vdW corrections to a standard GGA-DFT scheme.[49] This provides consistency with our recent calculations of bulk defects,[44] and sets the basis for future investigations of fs-laser-induced reconstructed domains[17] and other extended defective structures[16] on the surface of graphite.

It has recently been shown that the inclusion of site-specific vdW corrections,[54] higher order multipole,[55,56] or three-body contributions[57] can improve the accuracy of vdW-corrected GGA-DFT. However, to the best of our knowledge, no evidence exists regarding the performance of these methods with respect to graphite, diamond, and intermediate sp^2-sp^3 structures. The relatively simple scheme proposed in Ref. 49 (cDFT in the following) has already been tested[44] to yield: (i) the structural parameters and elastic constants for both diamond and graphite in close agreement with the experiment; (ii) the cohesive energy difference between graphite and diamond in semiquantitative accord with the experimental value; (iii) the strain-energy profile for distorted sp^3 structure (as expected for intrinsic defects in graphite) in close match with the screened hybrid DFT results; and (iv) the calculated diffusion barrier for surface vacancies (distorted sp^2 intermediates) in quantitative agreement with the experimental value (see also below). The successful outcome of these tests (not considered in Refs. 40, 49, 50, and 54–60) constitutes the motivation behind the choice of this method for the present study of surface defects.

The paper is organized as follows. In Sec. II we describe the cDFT method together with the simulation details. The results for isolated I, clustered interstitials and adatoms (I_2,I_3), isolated V, coupled vacancies (VV), and the intimate I-V Frenkel pair are reported and discussed in Sec. III. Section IV summarizes the main conclusion of this study.

II. METHODS

A. Empirical van der Waals corrections

We followed the general cDFT approach in implementing the long-range vdW energy term and its analytical gradient in a standard DFT scheme,[40,49,50,54–60]

$$E_{TOT} = E_{DFT} + E_{vdW}, \tag{1}$$

The long-range vdW energy term E_{vdW} was implemented into the VASP code,[61,62] by means of a real-space summation scheme including periodic boundary conditions,

$$E_{vdW} = -\frac{1}{2}\sum_{i,j} C_{6,ij}\left[\sum_{\boldsymbol{R}} \frac{f_{damp}(|\boldsymbol{r}_{ij}+\boldsymbol{R}|)}{|\boldsymbol{r}_{ij}+\boldsymbol{R}|^6}\right], \tag{2}$$

where $\boldsymbol{r}_{ij}=\boldsymbol{r}_i-\boldsymbol{r}_j$ is the interatomic distance, $\boldsymbol{R}=l\boldsymbol{a}+m\boldsymbol{b}+n\boldsymbol{c}$ are the lattice vectors ($l,m,n \in N$), and the coefficients $C_{6,ij}$ define the i-j specific pairwise interactions. A short-range damping function f_{damp} is introduced to eliminate the $|\boldsymbol{r}_{ij}+\boldsymbol{R}|^{-6}$ singularity as $|\boldsymbol{r}_{ij}+\boldsymbol{R}|\to 0$. Encouraged by the good performance of this method in consistently describing the properties of both diamond and graphite,[44,49] we followed Ref. 49 in defining both $C_{6,ij}$ and f_{damp}. In particular, the $C_{6,ij}$ parameters were defined on the basis of the London approximation for interatomic dispersion terms,

$$C_{6,ij} = \frac{3}{2}\alpha_i\alpha_j\frac{I_iI_j}{I_i+I_j}. \tag{3}$$

This allows calculating the $C_{6,ij}$ coefficients using experimental ionization potentials (I) and polarizabilities (α) for the atomic species i and j. In the present application we used the experimental values for carbon, i.e., $I_i=I_j=11.26$ eV and $\alpha_i=\alpha_j=1.76$ Å^{-3}.[63] For the damping function f_{damp}, we adopted the exponential decay function suggested in Ref. 49,

$$f_{damp}(|\boldsymbol{r}_{ij}+\boldsymbol{R}|) = 1-\exp[-\lambda\chi_{ij}^n],$$

$$\chi_{ij} = \frac{|\boldsymbol{r}_{ij}+\boldsymbol{R}|}{r_{cov}^i + r_{cov}^j} \tag{4}$$

with fixed value of $n=8$ and $\lambda=7.5\times10^{-4}$. In Eq. (4) the interatomic distance $|\boldsymbol{r}_{ij}+\boldsymbol{R}|$ is normalized to the sum of the covalent radii (r_{cov}) of the atoms i and j. As in Refs. 44 and 49 we used the experimental value of $r_{cov}=0.77$ Å.[63] Finally, the lattice summation over $\boldsymbol{R}$ in Eq. (2) was truncated enforcing a cut-off value of 100 Å.[44,60]

B. Computation details

The total energy and electronic structure were calculated using the VASP code and ultrasoft pseudopotentials.[61,62] The wave functions were expanded in plane waves according to the standard VASP implementation.[61,62] To compare with the results of previous plane-wave GGA calculations,[35] and with the cDFT results for bulk graphite,[44] we adopted a 286.7 eV cutoff in the simulation of defects. Increasing this value has been shown to yield negligible changes in the structure, formation energies and spin polarization of defects, and nearest interstitial-vacancy pairs in the bulk of graphite.[44] The exchange and correlation were included at PW91 level[64] and adopting the Vosko *et al.*[65] interpolation scheme.

Defects in graphite were modeled in a 4×4 trilayer slab adopting a $4\times4\times1$ (Γ-centered k-point grid, which was checked to yield results converged to within 3 meV with respect to an augmented $8\times8\times1$ k-point grid. The supercell size was chosen with the aim of identifying surface effects on the calculated structures and properties of intrinsic defects by comparison with previous bulk cDFT results obtained using cells with 4×4 in-plane periodicity.[44] As shown previously,[44] such lateral extension of the simulation cell provides a converged comparison among the energies for all the considered defects, the only exception being the intralayer grafted di-interstitial [I_2(7557) in the following]. Accordingly, the latter system was considered also in a larger 6×6 periodic cell (see below).

The convergence threshold adopted for geometry optimization was 0.01 eV Å^{-1}, which was also maintained for the

climbing nudged elastic band (cNEB) method[66] transition state search. All geometry optimizations were performed adopting the residual minimization method-direct inversion in the iterative subspace (RMM-DIIS)[67] algorithm as implemented in the VASP program.[61,62] To prevent artificial shear displacement of the layers during the optimization and transition state search, on each layer we kept the *xy* position of the atom farthest to the defect fixed in its optimized *AB*-stacked position. Both geometry optimization and cNEB calculations were performed accounting for spin polarization. The calculated spin polarization of the lowest-energy unsaturated adatom clusters was checked against the results of single-point (Γ-only) screened hybrid DFT [HSE06 (Refs. 68 and 69)], which confirmed the PW91 results.

Defect formation energies (E_f) were calculated as[70]

$$E_f = E_X - E_{slab} - N\mu_C, \tag{5}$$

where E_X is the total energy of the simulated slab with the defect X, and E_{slab} is the total energy for the defect-free graphite slab of the same size as for E_X. μ_C is the chemical potential of carbon, which was approximated with the cDFT energy of one carbon atom in bulk graphite.[35,44] N defines the number of atoms to be added ($N>0$) or removed ($N<0$) to create the defect X. Formation energies E_f are positive for all the considered defects and consequently the larger the E_f, the larger the energy stored in the given defect X.

The adsorption (incorporation) energy for isolated interstitials (adatoms) was calculated by adopting the energy of one isolated carbon atom in its triplet state [$E(^3C)$] as the energy reference for carbon,

$$E_{a(i)} = E_X - E_{slab} - NE(^3C), \tag{6}$$

where negative and positive values of $E_{a(i)}$ indicate exhothermic and endothermic processes, respectively.

III. RESULTS AND DISCUSSION

A. Graphite surface

Graphite consists of parallel layers, or graphene sheets, weakly bound together by vdW forces. Within individual layers, carbon atoms are arranged according to a honeycomb pattern with atomic bonds of 1.42 Å. This characteristic structure originates from the electronic π conjugation across the given graphene sheet.[71] Depending on the stacking sequence, graphite may occur in two structures: hexagonal (Bernal) *AB*-stacked graphite[72] and *ABC*-stacked rhombohedral graphite.[73] The predominant structure of highly oriented pyrolytic graphite (HOPG) is hexagonal (*AB*-stacked) graphite.[74] This structure is characterized by the presence of two nonequivalent atomic sites, which are usually referred to as α and β. While one carbon atom in the α site is sandwiched between two C atoms belonging to the adjacent layers, the β atom faces the center of the honeycomb structure of the neighboring layers.[72] This distinction applies also to the topmost HOPG layer which, accordingly, has two topologically nonequivalent sites [Fig. 1(a)].

Prior to simulating defects at the surface and subsurface of graphite, we checked the cDFT surface relaxation of a three-layer (four-layer) graphite slab with respect to the bulk of graphite. The optimized α-α (β-β) interlayer distances between the topmost and the second-topmost layers for the three- and four-layer slabs were 3.337 Å (3.340 Å) and 3.339 Å (3.340 Å), respectively. Thus, by comparison with the bulk interlayer separation of 3.345 Å (Ref. 44), we find negligible relaxation (−0.005/7 Å) and buckling (<0.002 Å) for the graphite surface. These results are in accordance with recent electron diffraction results for HOPG surfaces.[75]

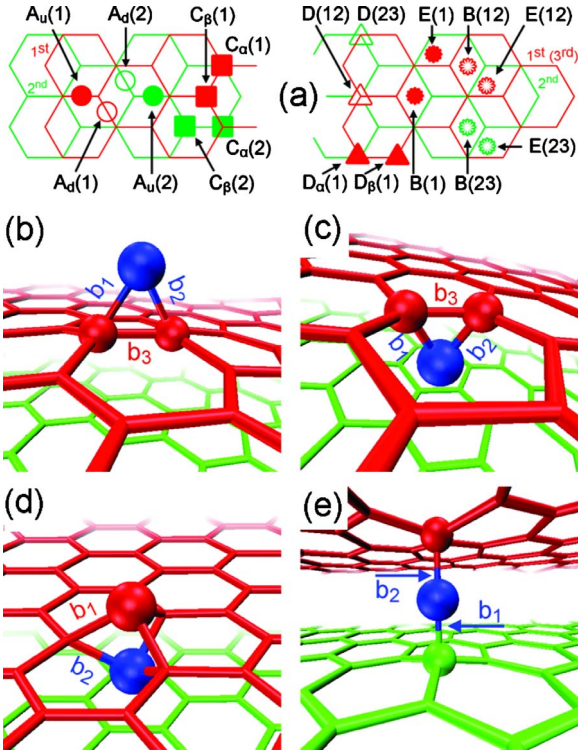

FIG. 1. (Color online) the initial positions of the interstitial (ad)atom together with the adopted labeling (a). Circles, squares, and triangles indicate A-like, C-like and D-like bondings, respectively. Unstable B and E configurations are shown as crimped dots. A-like interstitial (adatom) above (A_u) and below (A_d) the corresponding graphite layer are indicated as filled and empty circles, respectively. The same format has been used also to differentiate among the D-like defects. The Arabic numbers specify the graphite layer(s) onto which the defect is created starting from the topmost layer (1). In all panels, the topmost and second-topmost graphite layer is shown in gray (red) and light gray (green), respectively. Perspective views of the (b) A_u, (c) A_d, (d) C-like, and (e) D-like bondings follow. The interstitial (ad)atom is displayed as a dark gray (blue) sphere. Graphite atoms directly bonded to the extra carbon atom [(b), (c), and (e)] or displaced by it (d) have been also highlighted as spheres.

On the basis of the negligible deviations for the surface relaxation between the three- and four-layer slabs, the intrinsic defects were simulated in the thinner (three-layer) slab. Before moving to defects, we recall that while the stabilization (and coplanarity) of each graphene sheet in graphite originates from the σ and π bonding between carbon atoms on the same layer,[71] the vertical packing of graphene layers in graphite is mainly due to vdW interactions.[72–74] Thus, per-

turbations to the (σ) π bonding of a graphene sheet by a point defect may alter the electronic π conjugation of the layer and deform the ideal coplanarity. Once the coplanarity of a given layer is broken, the final geometry of a point-defect geometry results from a balance between the local bonding of the point defect and the energy penalty caused by both the reduced π conjugation and the changes in the optimum (vdW-governed) interlayer distance. Of course, the more extended the deformation on the defective layer, the larger its vdW energy penalty. Therefore, the interlayer vdW forces act to constrain the deformations which local rupture of the graphene (σ) π bonding brings about, effectively balancing covalent and nonbonding terms in graphite. Given the reduced vdW interactions experienced by the topmost layer of the graphite surface with respect to the subsurface and bulk layers, it is reasonable to expect that such covalent-vdW balance may change at the surface. In the following, we discuss how these changes affect the relative stability and properties of surface and subsurface defects in graphite.

B. Adatoms and subsurface interstitials

1. Defect structures

Carbon interstitial atoms are known to be produced by irradiation of graphite.[1–3,22–27] These have been previously and extensively studied in bulk graphite at LDA,[21] GGA,[35,36,41] and more recently vdW-corrected GGA (Refs. 40 and 44) level. However, to the best of our knowledge, no theoretical study has so far explicitly considered subsurface interstitials in comparison with bulk interstitials and surface adatoms.

To this end we calculated the structure of one extra carbon atom starting from several initial high-symmetry positions above and below different layers of the adopted graphite slab. Figure 1(a) displays the considered initial configurations. For ease of comparison with previous results for bulk graphite, we have adopted the same A–E labeling as in Refs. 35 and 44 and introduced an additional 1–3 labeling to differentiate the graphite layers.

Following the geometry optimization, all the initial A-like configurations converged into *grafted*[21] structures characterized by bonding of the extra atom to two (one α and one β) graphite atoms. As shown in Figs. 2(b) and 2(c) the extra carbon may sit either above (A_u) or below (A_d) one α-β graphite bond. Such a grafted interstitial-graphite bonding was obtained also as the result of relaxation of both the B and E initial configurations. Thus, similar to the bulk case,[44] cDFT suggests a barrier-less conversion of the B (E) structures into A_u (A_d), which makes the former unstable. Optimization of the C and D configurations also yielded two stable geometries. In the first one, the interstitial (adatom) sits directly above one β atom, which in turn is displaced either above or below the graphene plane [C_β in Figs. 1(a) and 1(d)]. In the second one, also known as the *Wallace* interstitial,[76] the interstitial binds vertically to two α carbons on the adjacent layers [Fig. 1(e)]. An analogous configuration, characterized by just one bond (b_1=1.76 Å, Table II), was obtained also for one adatom on the graphite surface.

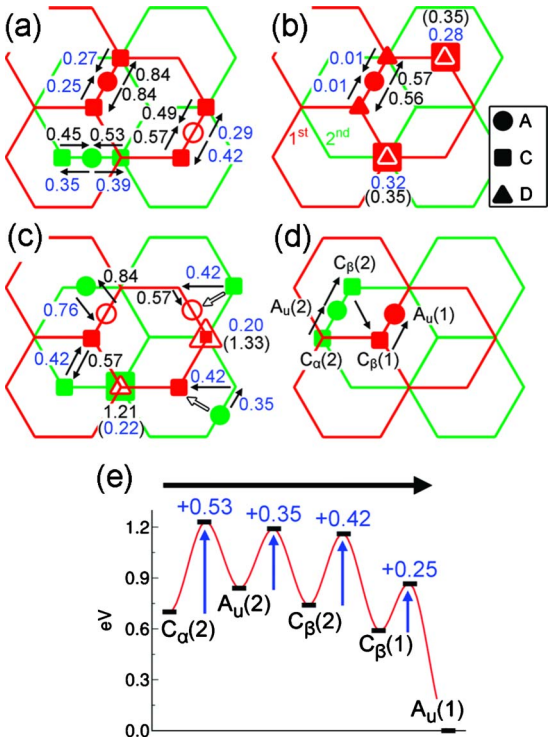

FIG. 2. (Color online) the considered elementary steps and corresponding cNEB barriers for the [(a) and (b)] in-plane and (c) interlayer diffusion of interstitial (ad)atoms. The barriers for the exothermic steps ($\Delta E<0$, see Table I) have been highlighted in dark gray (blue). (d) The lowest-energy path and corresponding energy profile (e) for the diffusion of subsurface interstitials toward the surface. The adopted labeling and graphical format are the same as in Fig. 1(a).

For completeness, we considered one interstitial (adatom) also in a C-like geometry above one α site (C_α), and D-like bonding for one adatom above one β carbon [$D_\beta(1)$]. Both of these geometries were found to be stable.

Thus, the simulations suggest several stable configurations for both interstitials and adatoms in graphite surface and subsurface regions. As shown in Table I, despite the similarities in bonding to the graphite lattice, we find the relative stabilities of these configurations to strongly depend on the vertical position in the modeled slab.

Specifically, the grafted adatom [$A_u(1)$,E_f=6.59 eV] is favored by more than 0.5 eV over the $C_{\alpha,\beta}(1)$ (E_f=7.15,7.18 eV) and $D_{\alpha,\beta}(1)$ (E_f=7.11,7.10 eV) configurations on the graphite surface. Localization of one grafted atom below the topmost layer [$A_d(1)$] results in a larger E_f (7.35 eV). However, when considered in the second-topmost layer, the relative energies of the interstitial configurations are inverted with respect to the surface case. In particular, the calculated E_f of 7.29 (7.33) eV for $C_\alpha(2)$ [$C_\beta(2)$] is lower than that for $A_u(2)$ (7.43 eV) and $A_d(2)$ (7.73 eV). In turn, these structures are calculated to be lower in energy than the Wallace D(12) (E_f=8.28 eV) and D(23) (E_f=8.40 eV) interstitials.

Notably, the calculated change in E_f going from $A_u(1)$ to $A_u(2)$ (+0.84 eV, Table I) is accompanied by a small change in the b_{1-3} bonds ($\leq$0.03 Å, Table II) but a substantial de-

TABLE I. Calculated formation (E_f, eV), adsorption (incorporation) ($E_{a(i)}$, eV) energy, and spin moment (μ_B, Bohr magnetons) for the optimized positions of carbon adatoms (1) and subsurface interstitial (2). The reader is referred to Fig. 1 for the adopted labeling. For comparison, cDFT results for the analogous configurations in bulk graphite [$A(b)$,$C_{\alpha,\beta}(b)$,$D(b)$] are also reported.

	E_f	$E_{a(i)}$	μ_B
$A_u(1)$	6.59	−1.35	0.3
$A_u(2)$	7.43	−0.51	0
$A_d(1)$	7.35	−0.59	0
$A_d(2)$	7.73	−0.21	0
$B(1)$	$A_u(1)$		
$B(12)$	$A_d(1)$, $A_u(2)$		
$B(23)$	$A_d(2)$		
$C_\alpha(1)$	7.15	−0.79	2
$C_\beta(1)$	7.18	−0.76	2
$C_\alpha(2)$	7.29	−0.65	2
$C_\beta(2)$	7.33	−0.61	2
$D_\alpha(1)$	7.11	−0.83	2
$D_\beta(1)$	7.10	−0.84	2
D(12)	8.28	0.34	1.2
D(23)	8.40	0.46	1.2
E(1)	$A_u(1)$		
E(12)	$A_d(1)$, $A_u(2)$		
E(23)	$A_d(2)$		
$A(b)$ [a]	8.06	0.12	0
$C_\alpha(b)$	7.93	−0.01	2
$C_\beta(b)$ [a]	7.89	−0.05	2
$D(b)$ [a]	8.87	0.93	1

[a]Reference 44.

crease (−0.16 Å) in the out-of-plane deformation (Δz, Table II) of the corresponding graphene layer. Thus, we find that the interlayer interactions act to constrain the A-induced relaxation of the graphite layer with the net effect of increasing the energy of subsurface A species with respect to C-like interstitials.

Moreover, despite the formation of two (shorter) covalent bonds (b_1=1.46 Å and b_2=1.47 Å in Table II), the calculated E_f for D(12) and D(23) is higher by more than 1 eV than that for $D_{\alpha,\beta}(1)$ (b_1=1.76,1.77 Å). Thus, the out-of-plane deformation (Δz=0.25–0.29 Å, Table II) of two, rather than one as for $D_{\alpha,\beta}(1)$, graphene sheets effectively compensates the energy gain introduced by formation of one extra bond (b_2). This, in turn, results in the larger E_f for D(12) and D(23) with respect to $D_{\alpha,\beta}(1)$.

These results suggest that the lower energy of adatoms with respect to interstitials stems from a subtle interplay between: (i) the number of bonds formed by the extra atom, (ii) the defect-induced relaxation allowed by the interlayer interactions, and (iii) the coplanarity of the given graphene sheet, which in turn affect its electronic π conjugation.

As a result, while the calculated E_f for the interstitial atoms (Table I) qualitatively follow the same trend as in the bulk of graphite [$E_f(A_{u,d}) > E_f(C_{\alpha,\beta}) > E_f(D)$], this is not the case for surface adatoms [$E_f(A_u) < E_f(C_{\alpha,\beta}) \simeq E_f(D)$]. These findings demonstrate that the bulk and subsurface interstitial models are not directly transferable to graphite adatoms. We speculate that these conclusions are likely to hold also for multilayer graphene.

TABLE II. Optimized bond lengths (b_{1-3},Å) for the stable configurations of subsurface interstitials and adatoms. The out-of-plane deformation induced by the adatom (interstitial) on the corresponding graphite layer(s) is indicated as Δz (Å). The reader is referred to Fig. 1 for the adopted labeling. For comparison, cDFT results for the analogous configurations in bulk graphite [$A(b)$,$C_{\alpha,\beta}(b)$,$D(b)$] are also reported.

	b_1	b_2	b_3	Δz
$A_u(1)$	1.53	1.53	1.54	0.45
$A_u(2)$	1.50	1.50	1.53	0.29
$A_d(1)$	1.50	1.50	1.53	0.39
$A_d(2)$	1.50	1.50	1.53	0.32
$C_\alpha(1)$	1.58(×3)	1.53(×3)		0.04
$C_\beta(1)$	1.58(×3)	1.53(×3)		0.05
$C_\alpha(2)$	1.55(×3)	1.55(×3)		0.01
$C_\beta(2)$	1.55(×3)	1.55(×3)		0.01
$D_\alpha(1)$	1.76			0.14, 0.01
$D_\beta(1)$	1.77			0.15, 0.01
D(12)	1.47	1.47		0.29, 0.29
D(23)	1.46	1.46		0.25, 0.27
$A(b)$ [a]	1.50	1.50	1.53	0.30
$C_\alpha(b)$	1.55(×3)	1.55(×3)		0.01
$C_\beta(b)$ [a]	1.55(×3)	1.55(×3)		0.01
$D(b)$ [a]	1.47	1.47		0.29, 0.29

[a]Reference 44.

Finally, given the negative adsorption (E_a) and incorporation (E_i) energies for the lowest-energy configurations of adatoms and interstitials (Table I), both processes turn out to be exothermic with the former being energetically favored over the latter. This suggests that, in principle, graphite surface could be also decorated via adsorption of gas-phase carbon.

2. Diffusion barriers

To investigate the mobility of adatoms and interstitials, we calculated also the in-plane and out-of-plane diffusion paths for both subsurface interstitials and adatoms. Figure 2 reports the considered elementary steps with the corresponding cNEB barriers.

For the in-plane diffusion [Figs. 2(a) and 2(b)], the simulations predict a relatively large barrier of 0.84 eV for diffusion of an $A_u(1)$ adatom into a $C_\alpha(1)$ [$C_\beta(1)$] position. Conversely, the largest calculated barrier in the second-topmost layer is only 0.53 eV. Thus, the simulations suggest the in-plane free diffusion of subsurface interstitials to be more facile than for surface adatoms. This originates from the increased stabilization of $A_u(1)$ with respect to the $A_u(1) \rightarrow C_\alpha(1)[C_\beta(1)]$ transition state, which makes detrapping from $A_u(1)$ energetically more expensive than diffusion

from $A_u(2)$ to $C_\alpha(2)[C_\beta(2)]$ [Tables I and II and Figs. 2(a) and 2(e)]. In addition, owing to the extremely small barrier (only 10 meV) for the $D_{\alpha,\beta}(1)$ conversion into $A_u(1)$, $D_{\alpha,\beta}(1)$ configurations should be considered as effectively unstable on the graphite surface at room temperature.

Turning to the interlayer diffusion of interstitials, the barrier for the $C_\beta(2) \rightarrow C_\beta(1)$ step (0.42 eV) turns out to be smaller than for other alternative steps such as $A_u(2) \rightarrow A_d(1)$ (0.76 eV) or $C_\alpha(2) \rightarrow D_\alpha(12)$ (1.21 eV). For completeness, we modeled also other elementary steps such as $C_\beta(2) \rightarrow A_d(1)$ and $A_u(2) \rightarrow C_\beta(1)$, which, however, converged onto the lowest-barrier $C_\beta(2) \rightarrow C_\beta(1)$ path [Fig. 2(c)].

We note that the barrier for free-interstitial in-plane diffusion [0.53 eV, Fig. 2(a)] is higher than for the lowest-energy interlayer migration step [$C_\beta(2) \rightarrow C_\beta(1)$, 0.42 eV in Fig. 2(c)]. Taking into account the lower E_f of adatoms (Table I), once the in-plane diffusion of interstitials is activated, their migration to the surface will be a spontaneous process [Fig. 2(e)].

Finally, we compare the results of our spin-polarized cDFT-cNEB calculations for isolated interstitials with the available spin-polarized GGA (Ref. 41) and spin-averaged cDFT data.[40] Although there is agreement on the calculated geometries, the formation energies differ qualitatively. In our calculations E_f for $A_u(1)$ is lower with respect to $C_{\alpha,\beta}(1)$, whereas in previous spin-averaged cDFT calculations for adatoms on graphene bilayer $E_f[A_u(1)] > E_f[C_\beta(1)]$.[40] Thus, similar to the case of bulk graphite,[44] the inclusion of spin polarization (neglected in Ref. 40) as well as vdW terms significantly affects the results for subsurface interstitials and adatoms. We also note that the cDFT $C_\beta(2)[C_\alpha(2)] \rightarrow A_u(2)$ barrier of 0.53 eV (0.45 eV) is in line with previous vdW-corrected GGA data [0.5 eV (Ref. 40)], and substantially lower than that calculated at spin-polarized GGA level for bulk graphite [0.9 eV (Ref. 41)]. Thus, the improved description of the balance between covalent and vdW interactions resulting from the inclusion of the vdW terms in the simulation, proves important also for the description of the diffusion of adatoms and subsurface (bulk) interstitials in graphite.

C. Subsurface di-interstitial

Interstitial clustering has been proposed as an important process in the evolution of radiation damage in graphite.[22–25,27] This process has been previously simulated at the LDA (Ref. 43) and cDFT (Ref. 44) levels in bulk graphite. However, to the best of our knowledge, no first-principles study has ever explicitly considered such defects in subsurface layers of graphite. To this end, we investigated several closest (I_2^1) and second-closest (I_2^2) interlayer interstitial pairs in subsurface layers of graphite. As shown in Fig. 3(a), these were designed on the basis of the lowest-energy A- and C-like stable configurations for subsurface interstitials (Table I).

Geometry optimization of the two C-like interstitials positioned in adjacent layers [$II^2(C_{\alpha,\beta})$, in Fig. 3(a)] did not lead to cluster formation but rather to coexistence of the two

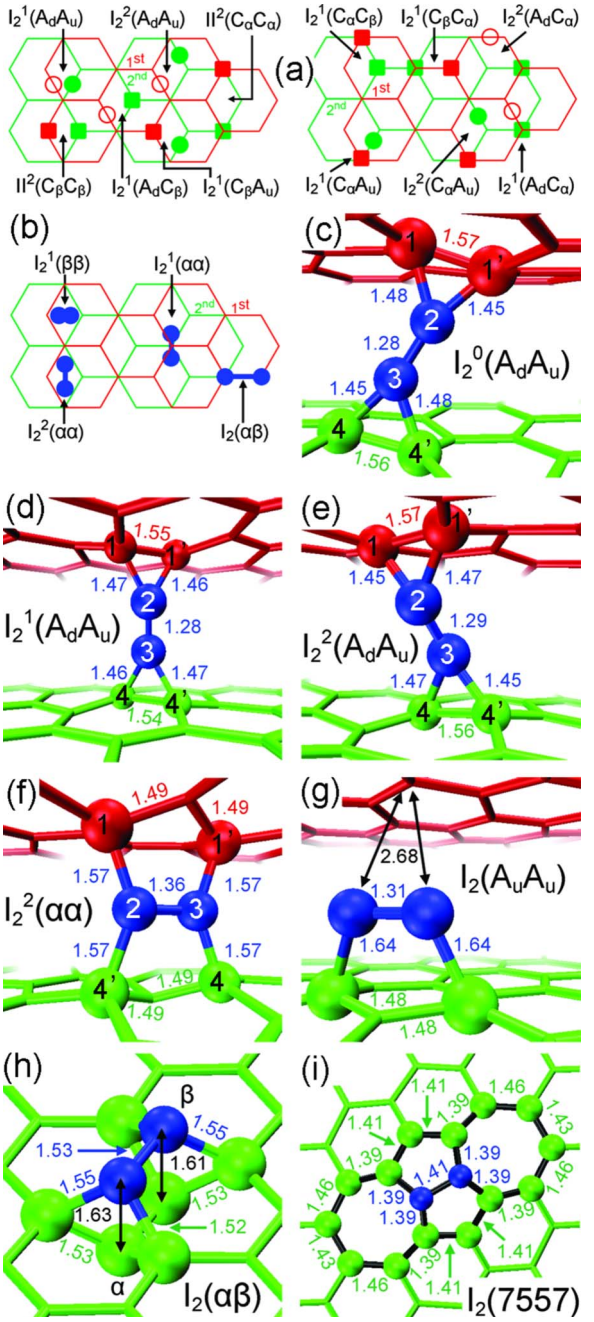

FIG. 3. (Color online) (a) The initial positions of close interstitial pairs and (b) di-interstitial I_2 dimer. Same graphical format as in Fig. 1(a). The I_2 dimer in (b) is displayed in dark gray (blue). Different labeling is used for unclustered (II) and clustered (I_2) configurations. The superscripts 0–2 refer to the interlayer distance between the interstitial atoms. The optimized stable structures are shown in panels (c)–(i) (see text for discussion). The I_2 dimer and the graphite atoms directly bonded to, or displaced by, I_2 are shown as spheres. Selected bond lengths are given in angstrom.

interstitials in a high-energy configuration ($E_f > 14$ eV, Table III). This originates from the rather large separation (>2.48 Å for all the considered II systems) between the interstitial atoms, which prevents spontaneous clustering.

Conversely, the relaxation of one A-like interstitial in the proximity of one C-like species resulted in spontaneous in-

TABLE III. Formation energy (E_f, eV) and calculated spin moment (μ_B, Bohr magnetons) for the optimized interstitial pairs displayed in Fig. 3. The net stabilization with respect to the corresponding isolated interstitials (Table I) is reported as ΔE_f (eV). Δz (Å) indicates the out-of-plane deformation induced by the di-interstitial on the topmost (1) and second-topmost (2) layers. For the configurations bound to both adjacent layers, the corresponding dihedral angles [1234 and 1′234′ in Figs. 3(c)–3(f)] are reported as Φ in degrees (°).

Initial	Relaxed	E_f (μ_B)	ΔE_f	$\Delta z(1,2)$	Φ
$I_2^1(A_dA_u)$	$I_2^1(A_dA_u)$	9.33 (0)	5.45	0.14, 0.27	49, 44
$I_2^2(A_dA_u)$	$I_2^2(A_dA_u)$	8.70 (0)	6.08	0.57, 0.60	1, 1.4
$I_2^1(A_dC_\alpha)$	$I_2^0(A_dA_u)$	8.90 (0)	5.74	1.58, 0.55	0, 0.01
$I_2^2(A_dC_\alpha)$	$I_2^2(A_dA_u)$				
$I_2^1(A_dC_\beta)$	$I_2^2(A_dA_u)$				
$I_2^1(C_\alpha A_u)$	$I_2^0(A_dA_u)$				
$I_2^2(C_\alpha A_u)$	$I_2^2(A_dA_u)$				
$I_2^2(C_\alpha C_\alpha)$	$II_2(C_\alpha C_\alpha)$	14.30 (0)	0.14	0.01, 0.01	
$I_2^1(C_\alpha C_\beta)$	$II^1(C_\alpha C_\beta)$	14.61 (4)	0.13	0.01, 0.01	
$I_2^1(C_\beta A_u)$	$I_2^2(A_dA_u)$				
$I_2^2(C_\beta C_\beta)$	$II^2(C_\beta C_\beta)$	14.50 (0)	0.01	0.01, 0.01	
$I_2^1(C_\beta C_\alpha)$	$II^1(C_\beta C_\alpha)$	14.60 (0)	0.14	0.01, 0.01	
$I_2^2(\alpha\alpha)$	$I_2^2(\alpha\alpha)$	9.75 (0)	5.03[a]	0.45, 0.45	
$I_2^1(\alpha\alpha)$	$I_2(A_uA_u)$	9.35 (0)	5.51	0.42, 0.25	0.5, 0.5
$I_2^2(\alpha\beta)$	$I_2^2(\alpha\beta)$	10.74 (0)	3.88	0.18, 0.03	
$I_2(7557)$	$I_2(7557)$	8.78 (0)	6.00	0.37, 1.75	

[a] ΔE_f calculated with respect to $A_d(1)+A_u(2)$ (Table I).

terstitial clustering and formation of a *twin-triangle*[43] configuration. This is characterized by a rather short bond (1.28–1.29 Å) between the two grafted A-like interstitials [$I_2^0(A_dA_u)$,$I_2^1(A_dA_u)$,$I_2^2(A_dA_u)$ in Fig. 3]. As shown in Table III, the calculated E_f for $I_2^2(A_dA_u)$ (8.70 eV) is by 0.20 eV and 0.63 eV lower than that for $I_2^0(A_dA_u)$ (8.90 eV) and $I_2^1(A_dA_u)$ (9.33 eV), respectively. We note that the bond lengths of the I_2 *dimer* remains practically constant for different configurations in Fig. 3, and that the induced out-of-plane layer deformation, Δz, is minimal for the highest energy $I_2^1(A_dA_u)$ configuration. The origin of the higher E_f of $I_2^1(A_dA_u)$ with respect to $I_2^0(A_dA_u)$ and $I_2^2(A_dA_u)$ can be explained by examining the dihedral angles (Φ) formed by the bonds of the I_2 dimer with the surrounding layers (Fig. 3). While Φ for $I_2^0(A_dA_u)$ and $I_2^2(A_dA_u)$ is quite small ($<1.5°$, Table III), this is not the case for $I_2^1(A_dA_u)$ ($\Phi>43°$). Thus, the nearly coplanar arrangement of the twin-triangle $I_2^0(A_dA_u)$ and $I_2^2(A_dA_u)$ configurations lowers their energy with respect to the more twisted $I_2^1(A_dA_u)$ geometry. In turn this result indicates the importance of the electronic π conjugation along the I_2 bonds for the cluster stabilization.

Building on the previous results in bulk graphite,[43,44] we considered also the possibility for the I_2 dimer to lie with its axis parallel to the graphite layers [Fig. 3(b)]. Apart from the $I_2^1(\beta\beta)$ case, which spontaneously converted into $I_2^2(A_dA_u)$, all these configurations have higher energies ($E_f>9.3$ eV in Table III). In spite of their coplanarity ($\Phi=0.5°$), the four I_2-*graphite* bonds of $I_2^2(\alpha\alpha)$ are now longer (+0.1 Å) than for $I_2^2(A_dA_u)$. Combined with the increased out-of-plane deformation of the surrounding layers ($\Delta z=0.45$ Å), this results in an increase by 1.05 eV of the calculated E_f for $I_2^2(\alpha\alpha)$ with respect to $I_2^2(A_dA_u)$.

We also considered a *grafted intralayer bridge* di-interstitial, which is characterized by two pentagonal and two hexagonal rings [$I_2(7557)$ in Fig. 3(i)], and is reminiscent of a Stone-Wales defect.[43] In spite of a substantial deformation of the corresponding graphite layer induced by the extra atoms (1.75 Å, Table III), this structure yields a surprisingly low E_f of only 8.78 eV. To further investigate the origin of the small difference in E_f (0.08 eV in Table III) between $I_2^2(A_dA_u)$ and $I_2(7557)$, and exclude possible finite-size effects, both configurations were optimized also in a 6×6 (14.73×14.73 Å^2) trilayer slab sampled with a $3\times3\times1$ k-point grid. Contrary to the calculations performed for the 4×4 slab, the obtained E_f for $I_2(7557)$ turned out to be by 0.2 eV lower than that for $I_2^2(A_dA_u)$. This results from the redistribution of the $I_2(7557)$-induced strain over the larger 6×6 layer which in turn leads to a reduced intralayer deformation amplitude (1.59 Å) with respect to the 4×4 cell case (1.75 Å). Thus, we find $I_2(7557)$ to be actually favored over $I_2^2(A_dA_u)$ in the subsurface region of graphite, which is in qualitative agreement with the previous results for bulk graphite.[43,44]

These results suggest that the stabilization of di-interstitials in subsurface layers of graphite results from a subtle balance between different interrelated factors: (i) the number of covalent bonds formed between the I_2 dimer and the graphite layers, (ii) the length of these bonds, (iii) their coplanarity, which in turn affects the electronic π conjugation along the atoms linking adjacent layers, (iv) the induced out-of-plane deformation of the surrounding layers, which also affects the π conjugation on the graphene layers, and (v) the interlayer interactions. Analogous to the bulk case,[21,35,44] we expect partial shearing of the graphite layers to complicate the interplay between these factors even further.

Finally, as shown in Table III, the large stabilization of the I_2 dimer with respect to two isolated interstitials [$\Delta E_f>5$ eV apart from the II-like configurations and $I_2(\alpha\beta)$] suggests that the subsurface clustering can compete with the surface migration (Fig. 2) in the thermal evolution of interstitials in graphite.

D. Adatom clusters

1. Dimers

As shown above (Fig. 2), diffusion of interstitials toward the surface is energetically favorable. Therefore we also considered the initial stages of surface adatoms clustering. As a starting point for geometry optimization we used several close-distance configurations designed on the basis of the lowest-energy A- and C-like bonded metastable adatoms [Fig. 4(a)].

Relaxation of two closest A_u adatoms [$2A_u$ in Fig. 4(a)] and of one A_u in the proximity of one C_α (C_β) adatom [C_α (C_β)+A_u in Fig. 4(a)] resulted in the spontaneous formation of an adatom I_2 dimer bonded in a grafted (A-like) way to

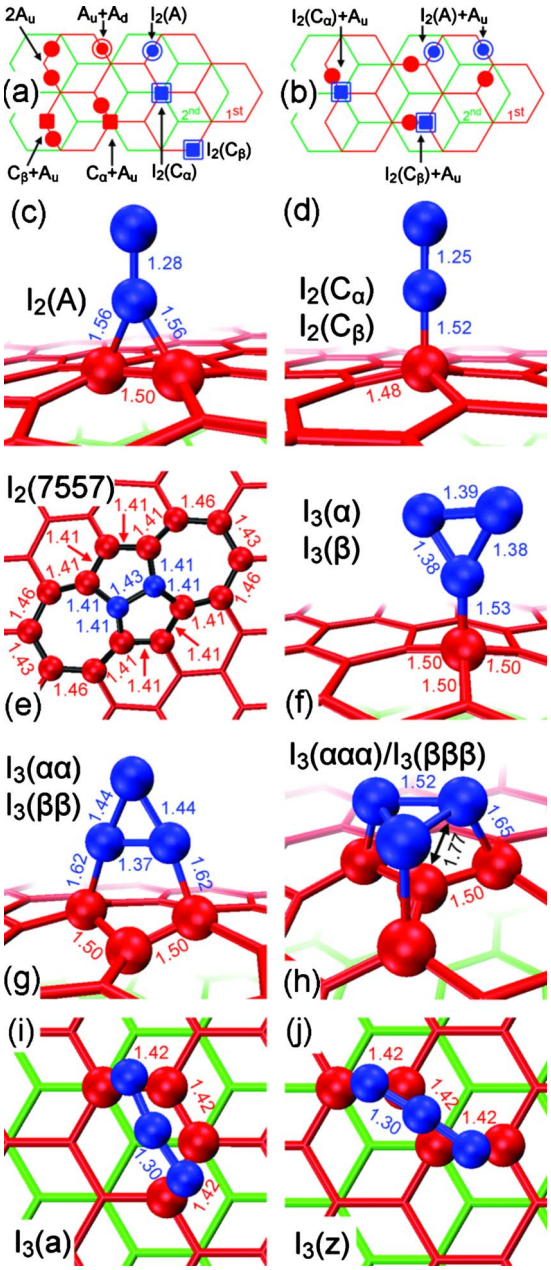

FIG. 4. (Color online) (a) The considered initial positions of the close adatom pairs and (b) I_2−dimer+adatom systems. Same graphical format as in Fig. 1(a). The A-like and C-like bound I_2 dimers are indicated by mean of dark gray (blue) circles and squares, respectively. Views of the optimized I_2-dimer and I_3-trimer structures follow in panels (c)–(e) and (f)–(j), respectively (see text for discussion). The I_2 (I_3) clusters and the graphite atoms directly bonded to, or displaced by, I_2 (I_3) have been displayed as spheres. Selected bond lengths are reported in angstrom.

the topmost layer [I_2(A) in Figs. 4(a) and 4(c)] with a formation energy (E_f) of 7.14 eV (Table IV).

Spontaneous dimer formation also occurred after optimizing the geometry of two A_u and A_d species grafted on the same C-C graphite bond [A_u+A_d in Fig. 4(a)]. In this case the dimer binds in a C-like configuration to one β carbon [$I_2(C_\beta)$ in Figs. 4(a) and 4(d)]. With a calculated E_f of 7.29 eV, this geometry is only 0.15 eV higher in energy than

TABLE IV. Formation energy (E_f, eV) and calculated spin moment (μ_B, Bohr magnetons) for the optimized adatom clusters displayed in Fig. 4. The net stabilization with respect to isolated A_u(1) adatoms (Table I) is reported as ΔE_f (eV). Δz (Å) indicates the out-of-plane deformation induced by the adatom cluster on the topmost graphite layer.

Initial	Relaxed	E_f	μ_B	ΔE_f	Δz
$2A_u$	I_2(A)	7.14	0(0[a])	6.04	0.40
C_α+A_u	I_2(A)				
C_β+A_u	I_2(A)				
A_u+A_d	$I_2(C_\beta)$	7.29	0(0[a])	5.89	0.45
$I_2(C_\alpha)$	$I_2(C_\alpha)$	7.33	0(0[a])	5.85	0.47
I_2(7557)	I_2(7557)	7.71	0	5.47	2.04
$I_2(C_\alpha)$+A_u	$I_3(\alpha)$	9.25	2(2[a])	10.52	0.48
$I_2(C_\beta)$+A_u	$I_3(\beta)$	9.27	2(2[a])	10.50	0.50
I_2(A)+A_u	$I_3(\alpha)$,$I_3(\beta)$				
$I_3(\alpha\alpha)$	$I_3(\alpha\alpha)$	10.84	0	8.93	0.56
$[I_3(\beta\beta)]$	$[I_3(\beta\beta)]$				
$I_3(\alpha\alpha\alpha)$	$I_3(\alpha\alpha\alpha)$	12.87	0	6.90	0.59
$[I_3(\beta\beta\beta)]$	$[I_3(\beta\beta\beta)]$				
$I_3(a)$	$I_3(a)$	8.70	0	11.07	0.03
$I_3(z)$	$I_3(z)$	8.70	0	11.05	0.04

[a]HSE06 functional.

I_2(A). Optimization of an analogous configuration above one α carbon [$I_2(C_\alpha)$ in Figs. 4(a) and 4(d)] led to a practically degenerate configuration (E_f=7.33 eV). Thus, as for isolated adatoms (Table I), we find A-like grafting to be favored over C-like bonding also for the adatom I_2 dimer.

We also considered the grafted intralayer bridge configuration on the graphite topmost layer [I_2(7557) in Fig. 4(e)]. Owing to the reduced vdW forces experienced by the topmost layer, the optimized I_2(7557) geometry is characterized by an increased out-of-plane deformation (Δz=2.04 Å in Table IV) and a lower E_f (7.71 eV) with respect to the subsurface case (Δz=1.75 Å, E_f=8.78 eV, Table III). However, contrary to the subsurface case, E_f for I_2(7557) is now considerably larger (~0.6 eV) than that for the lowest-energy I_2-dimer configuration {E_f[I_2(A)]=7.14 eV}. To check this result, we reconsidered the I_2 dimer in a larger 6×6 slab and obtained $E_f[I_2(7557)]-E_f[I_2(A)]$=0.4 eV, which confirms our conclusion. Thus, the absence of upper graphene layers, and the ensuing reduction in the vdW forces experienced by the topmost layer, allow for larger out-of-plane deformations (Δz), which in turn penalize the π conjugation of the corresponding layer. Altogether, these factors make local binding of the I_2 dimer [I_2(A),$I_2(C_{\alpha,\beta})$] favored over intralayer grafting [I_2(7557)] on the graphite surface. These results demonstrate that bulk and subsurface di-interstitial models are not directly transferable to adatom I_2 clusters.

The calculated barriers for the elementary $I_2(A)\rightarrow I_2(C_{\alpha,\beta})$ and $I_2(C_{\alpha,\beta})\rightarrow I_2(A)$ in-plane diffusion steps are ~0.35 eV and ~0.10 eV, respectively. Thus, we predict the in-plane diffusion of I_2 dimers to be more facile than for isolated adatoms (0.84 eV, Fig. 2). This originates

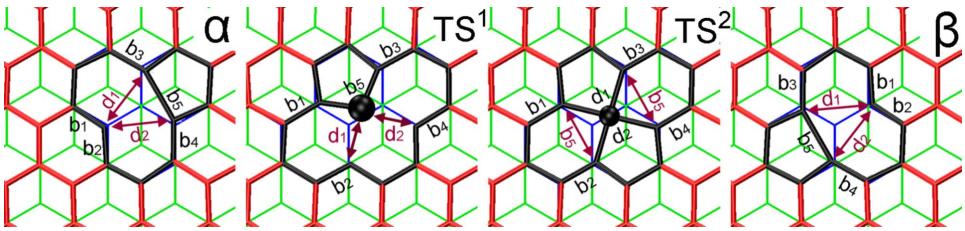

FIG. 5. (Color online) Top view of the optimized geometries for α vacancy (left) and β vacancy (right) in graphite. The modeled interconversion transition state for in-plane vacancy diffusion on the topmost (TS^1) and second-topmost (TS^2) layer are also displayed (middle). The *AB* stacking is highlighted by means of three different colors, namely, A: gray (red) and dark gray (blue), and B: light gray (green). The edges of the vacancy site have been highlighted as black lines. The atom involved in the $V(\alpha) \leftrightarrow V(\beta)$ interconversion is displayed as a black sphere in the central panels.

from: (i) the reduced number of bonds (five) involved in the $I_2(A) \leftrightarrow I_2(C_{\alpha,\beta})$ diffusion with respect to the adatom case [seven for $A_u(1) \leftrightarrow C_{\alpha,\beta}(1)$ in Figs. 1 and 2] and (ii) the smaller changes in the out-of-plane deformations (Δz) between the intermediate steps of diffusion (Tables II and IV).

2. Trimers

Given their relatively high mobility, it is reasonable to expect the I_2 dimers to diffuse on the surface and interact with other isolated adatoms. To model such a scenario, we considered also a third A_u adatom in the proximity of the lowest-energy $I_2(A)$ and $I_2(C_{\alpha,\beta})$ configurations [Fig. 4(b)]. In all cases the geometry optimization led to the spontaneous formation of a three-carbon cluster (I_3) bonded to just one α (β) graphite atom [$I_3(\alpha)$ and $I_3(\beta)$ in Fig. 4(f)]. With a calculated E_f of 9.25 and 9.27 eV, the two $I_3(\alpha)$ and $I_3(\beta)$ configurations turn out to be nearly degenerate.

To further investigate the bonding of the I_3 trimer to the graphite surface, we considered some alternative arrangements. These are reported in Figs. 4(g)–4(j). Initially, we investigated the bonding of the I_3 trimer via formation of two covalent bonds with two α (β) surface sites [$I_3(\alpha\alpha)$ and $I_3(\beta\beta)$ in Fig. 4(g)]. Despite the formation of two covalent bonds (1.62 Å) between the I_3 trimer and the surface, E_f for such geometry (10.84 eV) is 1.59 eV (1.57 eV) higher than those for $I_3(\alpha)$ [$I_3(\beta)$]. We also explored the possibility for a coplanar I_3 trimer to form three covalent bonds with the surface [$I_3(\alpha\alpha\alpha)$ and $I_3(\beta\beta\beta)$ in Fig. 4(h)], which resulted in an even higher energy configuration (E_f=12.87 eV).

Optimization of a linear I_3 trimer initially arranged along armchair [$I_3(a)$] and zigzag [$I_3(z)$] edges of the graphite surface resulted in spontaneous reorganization of the I_3 trimer in a vdW bound configuration physisorbed at roughly 3 Å above the topmost layer [Figs. 4(i) and 4(j)]. As shown in Table IV, with a calculated E_f of 8.70 and 8.72 eV for $I_3(a)$ and $I_3(z)$, the energies of both structures are practically degenerate and lower by roughly 0.5 eV than those for $I_3(\alpha)$ and $I_3(\beta)$.

Altogether these results suggest that the stabilization of I_3 trimers on graphite is not governed by the number of covalent bonds formed with the topmost layer, but rather by the ensuing perturbations on the π conjugation of the topmost layer. This stems from the fact that the sp^3 hybridization of the graphite atoms bound to the I_3 trimer (Fig. 4) results in their exclusion from the graphene π conjugation. This, in turn, tends to severely penalize the total energy of the I_3-graphite system (Table IV).

Finally, for all the considered cases, the formation of an adatom cluster from the isolated constituents leads to a substantial energy gain ($\Delta E_f > 5.4$ eV in Table IV), which is larger than for subsurface clusters (Table III) and increases going from the I_2 to the I_3 clusters. Thus, subsurface interstitials that are not trapped by subsurface clustering (Table III) or grain boundaries,[21] can be expected to diffuse to the surface upon annealing to eventually form adatom clusters (Tables I and IV and Fig. 2). Given the increased stabilization of I_3 over I_2, and the relatively low diffusion barrier for adatoms and I_2, it is reasonable to anticipate that, upon annealing, even larger cluster ($I_n, n>3$) may form on the surface of irradiated graphite samples.

E. Isolated vacancies

Carbon atom V are known to be generated by irradiation[1–3,22–28] or plasma treatment of graphite.[15,16] Owing to the *AB* stacking of hexagonal graphite,[72,73] removal of either one α or β carbon creates two topologically different V sites in graphite: α vacancy [$V(\alpha)$] and β vacancy [$V(\beta)$] shown in Fig. 5. Similar to the bulk,[44] the calculated E_f for V in the topmost (1) layer are almost identical i.e., 7.90 eV and 7.87 eV for $V^1(\alpha)$ and $V^1(\beta)$, respectively. Optimization of V in the second-topmost (2) layer [$V^2(\alpha), V^2(\beta)$] yields negligible deviations ($\leq$0.02 eV) with respect to [$V^1(\alpha), V^1(\beta)$] in terms of both the absolute and relative values of E_f. Thus, the simulations predict no marked difference between surface and subsurface vacancies. Yet, the calculated E_f for $V^{1,2}(\alpha,\beta)$ are roughly 0.7 eV lower than for bulk vacancies (Table V) and much closer to the experimental value of 7.0 ± 0.5 eV.[24] Given the negligible deviations between (sub)surface and bulk vacancies in terms of both in-plane (Table V) and interlayer distances (<0.03 Å), the difference in E_f is most likely due to electronic effects. We attribute such difference to the interlayer interactions, which have been previously shown to exist between vacancies in periodic models.[39] These interactions are absent in slab models with just one vacancy, as considered here. To confirm that this is indeed the main cause of the difference between the bulk and surface vacancy formation energies, one needs to investigate the dependence of the calculated E_f for multiple vacancies in graphite slabs thicker than the one adopted here. These results will be reported elsewhere.

TABLE V. Calculated formation energy (E_f, eV) and spin moment (μ_B, Bohr magnetons) for surface (1), subsurface (2), and bulk (b) carbon V. The relative energy of the $V(\alpha) \leftrightarrow V(\beta)$ transition state ($TS^{1,2}$) is reported with respect to energy of the α vacancy in the same layer [$V^1(\alpha)$ and $V^2(\alpha)$ for TS^1 and TS^2, respectively]. Representative bond lengths (b_{1-5} and d_{1-2}, Å) of the optimized geometries are also reported together with the induced out-of-plane deformation of the corresponding graphene layer (Δz, Å). The reader is referred to Fig. 5 for the adopted labeling. Optimized C-C bond length in perfect graphite: 1.42 Å.

	$V^1(\alpha)$	$V^1(\beta)$	$V^2(\alpha)$	$V^2(\beta)$	$V_b(\alpha)$ [a]	$V_b(\beta)$ [a]	TS^1	TS^2
E_f	7.90	7.87	7.92	7.88	8.62	8.58	+0.99	+1.43
μ_B	1.5	1.5	1.5	1.5	1.5	1.5	1	1
b_1	1.37	1.37	1.37	1.37	1.37	1.37	1.48	1.46
b_2	1.37	1.37	1.37	1.37	1.37	1.37	1.42	1.46
b_3	1.47	1.47	1.46	1.46	1.48	1.47	1.48	1.46
b_4	1.47	1.47	1.46	1.46	1.48	1.47	1.42	1.46
b_5	2.11	2.13	2.13	2.14	2.07	2.11	1.53	2.44
d_1	2.55	2.55	2.55	2.55	2.55	2.55	2.08	1.76
d_2	2.55	2.55	2.55	2.55	2.55	2.55	2.08	1.76
Δz	0.01	0.01	0.01	0.01	0.01	0.01	0.01	0.01

[a]Reference 44.

Regardless of the specific layer, the most stable geometries for both $V(\alpha)$ and $V(\beta)$ are planar and their symmetry is reduced from initial D_{3h} to C_{2v} point group.[21,34–37] The optimized geometry is characterized by the formation of one closed five-carbon ring, with an elongated bond length of 2.11–2.14 Å (b_5 in Fig. 5), and a pronounced reduction in the two C-C bonds opposite to the five-carbon ring (b_{1-2}=1.37 Å in Fig. 5). These findings are in quantitative agreement with earlier cDFT results for vacancies in bulk graphite[44] and demonstrate negligible differences in the geometry of V sites in surface, subsurface, and bulk-graphite regions. As for the bulk case,[44] and at odds with the results for V in single-layer graphene[36,37] and hydrogen saturated polyaromatic hydrocarbons,[34] we found negligible out-of-plane distortions (Δz=0.01 Å, Table V) for the lowest-energy configurations of both surface and subsurface vacancies.

The calculated barrier for the $V^1(\alpha) \leftrightarrow V^1(\beta)$ interconversion is 0.99 eV (1.02 eV) with respect to $V^1(\alpha)$ [$V^1(\beta)$], which is in close agreement with the experimental value of 0.9–1.0 eV for vacancy diffusion on the graphite surface.[16] The calculated barrier for the subsurface $V^2(\alpha) \leftrightarrow V^2(\beta)$ interconversion is +1.43 eV (+1.47 eV) with respect to $V^2(\alpha)$ [$V^2(\beta)$]. These values closely match the calculated bulk vacancy migration barriers of 1.40 eV (1.44 eV) with respect to the energies of bulk $V_b(\alpha)$ [$V_b(\beta)$].[44] Thus, the interlayer vdW interactions effectively increase the energy of the transition state for the subsurface vacancy in-plane diffusion.

It is interesting to note that the migration of the vacancy in the topmost layer takes place via an asymmetric transition state (TS^1 in Fig. 5). This state is characterized by asymmetric binding of the moving atom to just one side of the vacancy edge (b_5=1.53 Å and d_1=d_2=2.08 Å in Fig. 5). Conversely, the transition state in the second-topmost layer (TS^2) has a more symmetric configuration, in which the moving atom is symmetrically bound to both sides of the vacancy edge (d_1=d_2=1.76 Å), as previously found for V in bulk graphite.[44] This results from the different covalent-vdW balance at the topmost layers, which changes the energy surface experienced by the moving atom with respect to the bulk and subsurface cases. On this basis, it turns out that the balance between covalent and vdW terms is crucial also for isolated vacancies in graphite.

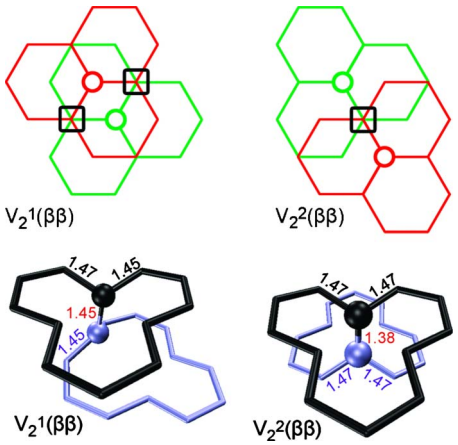

FIG. 6. (Color online) Top view of the considered interlayer (β) divacancies on the graphite surface (top panels). Intersections represent carbon atoms, and vacancy sites are indicated by empty circles. Same color labeling as in Fig. 1(a). The superscripts 1 and 2 denote first and second interlayer neighbors. Potential bonding sites have been marked by black squares. For $V_2^1(\beta\beta)$, only one of the two possible bonds is formed. Perspective view of the optimized geometries follows in the bottom panels. The edges of the upper and lower vacancy sites have been reported as black (black) and gray (cyan) lines. Selected bond lengths are reported in angstrom.

In order to investigate the interlayer diffusion of isolated vacancies, we calculated also the $V^2(\alpha) \leftrightarrow V^1(\alpha)$ interconversion barrier. In doing so, we fixed the xyz position of the atom farthest to the vacancy on each layer. The calculated barrier is 7.95 eV with respect to $V^2(\alpha)$. This result suggests that vacancies can hardly diffuse across the layers. Accordingly, such process is expected to minimally contribute to the experimentally measured thermal evolution of isolated vacancies on graphite surfaces.[16]

F. Divacancies

The interaction of vacancies in adjacent graphite layers via interlayer bonding has been proposed as a plausible explanation for the high migration barrier measured for vacancies in bulk graphite [3.1 ± 0.5 eV (Refs. 21 and 24)]. In addressing the transferability of bulk divacancy models to surface graphite, we limited our analysis to the closest interlayer divacancies capable of promoting interlayer bonding.[21,44] These are displayed in Fig. 6 and labeled in the same way as in Refs. 21 and 44.

As in the bulk case,[21,44] we find that the interaction of both the first [$V_2^1(\beta\beta)$ in Fig. 6] and the second-nearest interlayer neighbor vacancies [$V_2^2(\beta\beta)$] promotes interlayer

TABLE VI. Calculated formation energies (E_f, eV), and spin moment (μ_B, Bohr magnetons) for interlayer divacancies at the graphite surface (see Fig. 6). ΔE_f indicates the calculated stabilization energy with respect to two noninteracting $V^1(\beta)$ and $V^2(\beta)$ vacancies (Table V). Δz (Å) is the induced out-of-plane deformation on the two adjacent layers. The results for the analogous systems in bulk graphite (Ref. 44) are reported within brackets for comparison.

	E_f	ΔE_f	μ_B	Δz
$V_2^1(\beta\beta)$	14.27 (15.07)	1.48(2.09)	0(0)	1.01, 1.01(1.00, 1.01)
$V_2^2(\beta\beta)$	12.85 (13.66)	2.90(3.50)	0(0)	1.14, 1.10(1.10, 1.10)

bonding also on the graphite surface. The formation energies (E_f) for $V_2^1(\beta\beta)$ and $V_2^2(\beta\beta)$ are 14.27 eV and 12.85 eV, respectively. Considering that the sum of E_f for the isolated $V^1(\beta)$ and $V^2(\beta)$ is 15.75 eV (7.87+7.88 eV, Table V), the net stabilization energy (ΔE_f) is 1.48 eV and 2.90 eV for $V_2^1(\beta\beta)$ and $V_2^2(\beta\beta)$, respectively. Thus, despite the substantial deformation of the graphite layers ($\Delta z \sim 1$ Å, Table VI), the vacancy interlayer clustering is energetically favorable also on the graphite surface. However, the calculated stabilization energy for surface divacancies is significantly smaller ($\leq$0.6 eV, Table VI) than for the corresponding systems in the bulk of graphite.[44] This result reiterates the importance of interlayer interactions for the net stabilization of vacancies in periodic graphite models (Tables V and VI and Ref. 39).

As shown in Fig. 6, the calculated interlayer bond lengths are 1.45 Å and 1.38 Å for $V_2^1(\beta\beta)$ and $V_2^2(\beta\beta)$, respectively. These values are in close agreement with the bulk values of 1.46 Å and 1.38 Å.[44] Thus, despite the changes in E_f and ΔE_f, the optimized geometries of both surface $V_2^1(\beta\beta)$ and $V_2^2(\beta\beta)$ divacancies are found to closely match the bulk results.[44]

As noted above, the stabilization of divacancies by interlayer bonding provides a plausible explanation to the experimental vacancy migration barrier of 3.1 ± 0.5 eV in bulk graphite.[21,24,44] Assuming that vacancies in graphite migrate by interconversion between $V_2^2(\beta\beta)$ and $V_2^1(\beta\beta)$, the net barrier for vacancy migration can be estimated by summing up the calculated difference in formation energies (14.27−12.85=1.42 eV, Table VI) with the lowest diffusion barrier for monovacancies in the topmost layers (0.99 eV, Table V). The resulting value of 1.42+0.99=2.41 eV is lower than similar cDFT bulk estimates [2.85 eV (Ref. 44)] and the experimental data [3.1 ± 0.5 eV (Ref. 24)] for bulk graphite.

In addition, detrapping from $V_2^1(\beta\beta)$ would cost (at least) the $V_2^1(\beta\beta)$ stabilization (ΔE_f=1.47 eV, Table VI) plus the surface monovacancy migration barrier (0.99 eV, Table V), yielding a final value of 1.47+0.99=2.46 eV, which is considerably lower than similar cDFT bulk estimates [3.53 eV (Ref. 44)].

These results demonstrate that, despite the fairly good agreement on the optimized geometries, the calculated stabilization and detrapping energies for surface divacancies are noticeably lower than in the bulk. On this basis, the transferability of bulk divacancy models to the surface is found to be rather poor.

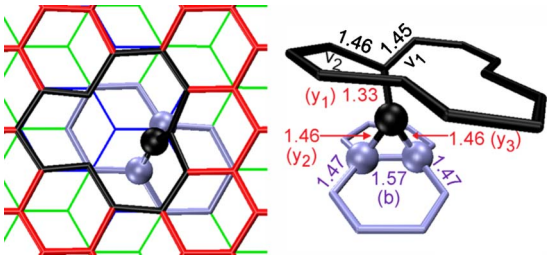

FIG. 7. (Color online) Top (left) and perspective (right) view of the optimized geometry for the intimate Frenkel (I-V) pair on graphite surface. The topmost, second-topmost, and third layers are displayed in gray (red), light gray (green), and dark gray (blue), respectively. The edges of the upper vacancy site and the two lower layer rings closest to the interstitial atom have been highlighted as thick black (black) and light gray (cyan) lines. Selected bond lengths are reported in angstrom.

G. Intimate Frenkel pairs

Finally, we consider the formation energies and structures of the intimate I-V Frenkel pairs on the graphite surface. The formation of I-V pairs has been proposed in irradiated graphite and they have been the subject of intense experimental[22–26] and theoretical studies.[21,35,41,42,44] These studies focused on the origin of the energy release peak from irradiated samples at 200 °C.[22,25] In particular, the recombination barrier of close I-V pairs ($\sim$1 eV) has been recently shown to match the experimental value of 1.38 ± 0.2 eV (Ref. 22) and 0.89 ± 0.10 eV (Ref. 26) measured for electron irradiated and He^+ bombarded graphite, respectively.[21,44]

Building on previous extensive investigations of possible I-V metastable configurations in bulk graphite,[44] here we limited our analysis to the most stable intimate I-V pair [$V(\beta)-I(br_0)$ in Ref. 44]. The optimized geometry for the intimate I-V pair is shown in Fig. 7. It is a *y*-shaped (ylid[21,42]) configuration in which the I atom forms a rather short (y_1=1.33 Å) bond with one layer, and two longer ($y_2=y_3$=1.46 Å) bonds with the adjacent graphite layer. Its formation energy (E_f) is 10.75 eV, which is by 0.76 eV smaller than for the analogous configuration in hexagonal bulk graphite [E_f=11.51 eV (Ref. 44)]. Thus, although more favorable than an isolated $A_u(1)$ [$A_d(1)$, Table I] interstitial and an isolated vacancy $V^1(\beta)$ (Table V) by 3.71 eV (4.47 eV), the energy of the intimate I-V pair is smaller on the surface than in the bulk.

In order to assess the actual stability of intimate I-V pair we studied also its recombination into perfect hexagonal graphite. The calculated recombination barrier (E_b) is 1.23 eV, i.e., larger by roughly 0.2 eV than that for the corresponding bulk case [E_b=1 eV (Ref. 44)]. Thus, we find that the reduced vdW interactions experienced by the surface I-V pair alter the potential energy surface governing the I-V recombination. In turn, this results in a higher energy transition state with respect to the bulk case.

H. Magnetic properties

Performing spin-polarized calculations allows us to discuss the magnetic properties of the considered systems. We start from isolated interstitial (adatom) species (see Table I).

Regardless of its localization, the C-like configuration is calculated to have a net magnetic moment of 2 μ_B. As already shown for the bulk case,[44] the calculated magnetic moment originates from the occurrence of two spin-polarized electronic states just below the Fermi level, which are partially delocalized over the α (β) carbon network around the C(α) [C(β)] site.

Conversely to the C-like case, we find a nonmagnetic (0 μ_B) solution for all the subsurface A-like configurations (Table I). We also find a partially spin-polarized (0.3 μ_B) solution for the $A_u(1)$ configuration, which qualitatively recovers the previous result for the analogous configuration on a single graphene layer [0.5 μ_B (Ref. 77)]. These findings strengthen previous arguments regarding the importance of interlayer interactions in determining the properties of intercalated species in graphite.[44]

Turning to isolated carbon V, we find analogies between cDFT data and previous results for isolated V in graphene and bulk graphite.[36,38,39,44] Formation of the five-carbon ring is consistently found to partially saturate two of the three dangling bonds associated with the vacancy. This leads to accumulation of spin density on the (undercoordinated) atom opposite to the five-ring (see Fig. 6 in Ref. 44) and a calculated magnetic moment (~1.5 μ_B), in line with previously published results for the same defect concentration.[38,39]

Similar to the bulk case,[44] we find that pairing of interstitials, adatoms, vacancies, as well as interstitials with vacancies tends to quench the magnetic properties of the isolated defects by either saturating their dangling bonds (Tables III and VI) or generating singlet (0 μ_B) spin states which HSE06 results confirm as representative (Table IV). Since such pairing is calculated to be energetically favorable (Tables III, IV, and VI), we expect that, in the absence of hydrogen contamination,[36] most of the defects in irradiated samples will tend to form nonmagnetic superstructures (adatom, I, and V clusters and close I-V pairs) and, accordingly, lead to feeble magnetic signals for irradiated samples. One can also assume that the facile interstitial diffusion (Fig. 2) may lead to saturation of the dangling bonds present at grain boundaries,[30,31] thus quenching also the magnetic signal associated with these sites.[31] On this basis, we suggest that the almost negligible magnetic signal measured from He-irradiated graphite samples[11] may originate from: (i) aggregation and eventual magnetic quenching of isolated (initially spin-polarized) defects and (ii) saturation of spin-polarized electrons at grain boundaries[31] by interstitials-based species. Taking advantage of the numerical efficiency of the adopted cDFT method, work is currently in progress to further investigate the latter hypothesis.

IV. CONCLUSIONS

One can summarize the main results of our investigation of intrinsic defects in graphite surface and subsurface regions by spin-polarized vdW-corrected DFT as follows:

(i) the formation energy (E_f) of adatoms is lower than E_f of subsurface I atoms.

(ii) Despite analogies in the bonding to the graphite lattice, the relative stabilities of different configurations of subsurface I atoms and surface adatoms are different.

(iii) The diffusion of subsurface I atoms to the graphite surface is energetically favorable and is governed by relatively low barriers (~0.5 eV).

(iv) The barrier for in-plane free diffusion of adatoms (0.84 eV) is larger than for in-plane and interlayer migration of I atoms (~0.5 eV).

(v) Clustering of both I atoms and adatoms is energetically favorable. The simulations suggest lower formation energies for surface diadatoms than for subsurface di-interstitials.

(vi) The differences in the structure and diffusion barriers of intrinsic defects on the surface and in subsurface region of graphite originate from a complex interplay among several factors including the number, strain, and orientation of the covalent bonds formed with the graphite lattice and the induced out-of-plane deformation on the adjacent graphene sheets, which in turn affect both their π conjugation and the interlayer vdW interaction.

(vii) Due to the surface truncation and to the reduced vdW interaction experienced by the topmost layer, the balance between covalent and nonbonding terms for surface defects is different from that in subsurface and bulk graphite. As a result, in spite of analogies in the bonding to the graphite lattice, the transferability of bulk defect models to the graphite surface is generally rather poor in terms of both relative stabilities and diffusion barriers. Accordingly, the interpretation of surface data on the basis of bulk-graphite models may lead to misleading conclusions.

(viii) The energetically advantageous pairing of isolated defects (I, V, adatoms) effectively saturates residual dangling bonds, thus quenching the defect induced spin polarization in damaged graphite surfaces.

ACKNOWLEDGMENTS

This work was supported by a specially promoted Grant-in-Aid for Scientific Research (Contract No. 19001002) from the Ministry of Education, Culture, Sports, Science and Technology of Japan. This work made use of the facilities of HECToR, the U.K.'s national high-performance computing service, which is provided by UoE HPCx Ltd. at the University of Edinburgh, Cray Inc. and NAG Ltd., and funded by the Office of Science and Technology through EPSRC's High End Computing Programme. The authors also acknowledge the use of the UCL Legion High Performance Computing Facility, and associated support services, in the completion of this work.

*g.teobaldi@ucl.ac.uk

[1] T. Tanabe, Phys. Scr. **T64**, 7 (1996).
[2] J. H. W. Simmons, *Radiation Damage in Graphite* (Pergamon, London, 1965).
[3] L. Arnold, *Windscale 1957: Anatomy of a Nuclear Accident* (Palgrave MacMillan, London, 1995).
[4] A. V. Krasheninnikov and F. Banhart, Nature Mater. **6**, 723 (2007).
[5] P. Avouris, Z. Chen, and V. Perebeinos, Nat. Nanotechnol. **2**, 605 (2007).
[6] I. Žutić, J. Fabian, and S. Das Sarma, Rev. Mod. Phys. **76**, 323 (2004).
[7] M. S. Kane, L. C. Kao, R. K. Mariwala, D. F. Hilscher, and H. Foley, Ind. Eng. Chem. Res. **35**, 3319 (1996).
[8] G. Mestl, N. I. Maksimova, N. Keller, V. V. Roddatis, and R. Schlögl, Angew. Chem., Int. Ed. **40**, 2066 (2001).
[9] A. Hashimoto, K. Suenaga, A. Gloter, K. Urita, and S. Iijima, Nature (London) **430**, 870 (2004).
[10] P. Esquinazi, D. Spemann, R. Höhne, A. Setzer, K. H. Han, and T. Butz, Phys. Rev. Lett. **91**, 227201 (2003).
[11] K. H. Han, D. Spemann, P. Esquinazi, R. Höhne, V. Riede, and T. Butz, Adv. Mater. **15**, 1719 (2003).
[12] Y. Ferro, C. Thomas, T. Angot, P. Génésio, and A. Allouche, J. Nucl. Mater. **363-365**, 1206 (2007).
[13] J. R. Hahn and H. Kang, Phys. Rev. B **60**, 6007 (1999).
[14] B. Rosseau, H. Estrade-Szwarckopf, A. L. Thomann, and P. Brault, Appl. Phys. A: Mater. Sci. Process. **77**, 591 (2003).
[15] J. I. Paredes, A. Martinez-Alonso, and J. M. D. Tascón, Carbon **38**, 1183 (2000).
[16] J. I. Paredes, P. Solís-Fernández, A. Martinez-Alonso, and J. M. D. Tascón, J. Phys. Chem. C **113**, 10249 (2009).
[17] J. Kanasaki, E. Inami, K. Tanimura, H. Ohnishi, and K. Nasu, Phys. Rev. Lett. **102**, 087402 (2009).
[18] M. B. Agranat, S. I. Ashitkov, V. E. Fortov, S. I. Anisimov, A. M. Dykhne, and P. S. Kondratenko, J. Exp. Theor. Phys. **88**, 370 (1999).
[19] S. Amoruso, G. Ausanio, M. Vitiello, and X. Wang, Appl. Phys. A: Mater. Sci. Process. **81**, 981 (2005).
[20] M. Lenner, A. Kaplan, and R. E. Palmer, Appl. Phys. Lett. **90**, 153119 (2007).
[21] R. H. Telling, C. P. Ewels, A. A. El-Barbary, and M. I. Heggie, Nature Mater. **2**, 333 (2003).
[22] E. W. J. Mitchell and M. R. Taylor, Nature (London) **208**, 638 (1965).
[23] G. W. Hinman, A. Haubold, J. O. Gardner, and J. K. Layton, Carbon **8**, 341 (1970).
[24] P. A. Thrower and R. M. Mayer, Phys. Status Solidi A **47**, 11 (1978).
[25] T. Iwata, J. Nucl. Mater. **133-134**, 361 (1985).
[26] E. Asari, M. Kitajima, K. G. Nakamura, and T. Kawabe, Phys. Rev. B **47**, 11143 (1993).
[27] K. Niwase, Phys. Rev. B **52**, 15785 (1995).
[28] M. M. Ugeda, I. Brihuega, F. Guinea, and J. M. Gómez-Rodríguez, Phys. Rev. Lett. **104**, 096804 (2010).
[29] B. J. Albers, T. C. Schwendemann, M. Z. Baykara, N. Pilet, M. Liebmann, E. I. Altman, and U. D. Schwarz, Nat. Nanotechnol. **4**, 307 (2009).
[30] Y. Lu, M. Muñoz, C. S. Steplecaru, C. Hao, M. Bai, N. Garcia, K. Schindler, and P. Esquinazi, Phys. Rev. Lett. **97**, 076805 (2006).
[31] J. Červenka, M. I. Katsnelson, and C. F. J. Flipse, Nat. Phys. **5**, 840 (2009).
[32] J. H. Warner, M. H. Rümmeli, L. Ge, T. Gemming, B. Montanari, N. M. Harrison, B. Büchner, and G. A. D. Briggs, Nat. Nanotechnol. **4**, 500 (2009).
[33] J. Kibsgaard, J. V. Lauritsen, E. Lægsgaard, B. S. Clausen, H. Topsøe, and F. Besenbacher, J. Am. Chem. Soc. **128**, 13950 (2006).
[34] A. A. El-Barbary, R. H. Telling, C. P. Ewels, M. I. Heggie, and P. R. Briddon, Phys. Rev. B **68**, 144107 (2003).
[35] L. Li, S. Reich, and J. Robertson, Phys. Rev. B **72**, 184109 (2005).
[36] P. O. Lehtinen, A. S. Foster, Y. Ma, A. V. Krasheninnikov, and R. M. Nieminen, Phys. Rev. Lett. **93**, 187202 (2004).
[37] Y. Ma, P. O. Lehtinen, A. S. Foster, and R. M. Nieminen, New J. Phys. **6**, 68 (2004).
[38] O. V. Yazyev and L. Helm, Phys. Rev. B **75**, 125408 (2007).
[39] R. Faccio, H. Pardo, P. A. Denis, R. Y. Oeiras, F. M. Araújo-Moreira, M. Veríssimo-Alves, and A. W. Mombrú, Phys. Rev. B **77**, 035416 (2008).
[40] Y. Ma, Phys. Rev. B **76**, 075419 (2007).
[41] O. V. Yazyev, I. Tavernelli, U. Rothlisberger, and L. Helm, Phys. Rev. B **75**, 115418 (2007).
[42] C. P. Ewels, R. H. Telling, A. A. El-Barbary, M. I. Heggie, and P. R. Briddon, Phys. Rev. Lett. **91**, 025505 (2003).
[43] C. D. Latham, M. I. Heggie, J. A. Gámez, I. Suárez-Martínez, C. P. Ewels, and P. R. Briddon, J. Phys.: Condens. Matter **20**, 395220 (2008).
[44] G. Teobaldi, H. Ohnishi, K. Tanimura, and A. L. Shluger, Carbon **48**, 4145 (2010).
[45] H. Rydberg, M. Dion, N. Jacobson, E. Schröder, P. Hyldgaard, S. I. Simak, D. C. Langreth, and B. I. Lundqvist, Phys. Rev. Lett. **91**, 126402 (2003).
[46] D. C. Langreth, B. I. Lundqvist, S. D. Chakarova-Käck, V. R. Cooper, M. Dion, P. Hyldgaard, A. Kelkkanen, J. Kleis, L. Kong, S. Li, P. G. Moses, E. Murray, A. Puzder, H. Rydberg, E. Schröder, and T. Thonhauser, J. Phys.: Condens. Matter **21**, 084203 (2009).
[47] G. Román-Pérez and J. M. Soler, Phys. Rev. Lett. **103**, 096102 (2009).
[48] S. Fahy, S. G. Louie, and M. L. Cohen, Phys. Rev. B **34**, 1191 (1986).
[49] F. Ortmann, F. Bechstedt, and W. G. Schmidt, Phys. Rev. B **73**, 205101 (2006).
[50] M. Hasegawa and K. Nishidate, Phys. Rev. B **70**, 205431 (2004).
[51] G. Kern and J. Hafner, Phys. Rev. B **58**, 13167 (1998).
[52] K. R. Kganyago and P. E. Ngoepe, Mol. Simul. **22**, 39 (1999).
[53] H. Rydberg, N. Jacobson, P. Hyldgaard, S. I. Simak, B. I. Lundqvist, and D. C. Langreth, Surf. Sci. **532-535**, 606 (2003).
[54] A. Tkatchenko and M. Scheffler, Phys. Rev. Lett. **102**, 073005 (2009).
[55] A. D. Becke and E. R. Johnson, J. Chem. Phys. **127**, 154108 (2007).
[56] S. N. Steinmann and C. Corminboeuf, J. Chem. Theory Comput. **6**, 1990 (2010).
[57] O. A. von Lilienfeld and A. Tkatchenko, J. Chem. Phys. **132**, 234109 (2010).
[58] Q. Wu and W. Yang, J. Chem. Phys. **116**, 515 (2002).
[59] S. Grimme, J. Comput. Chem. **27**, 1787 (2006).

[60] V. Barone, M. Casarin, D. Forrer, M. Pavone, M. Sambi, and A. Vittadini, J. Comput. Chem. **30**, 934 (2009).
[61] G. Kresse and J. Furthmüller, Phys. Rev. B **54**, 11169 (1996).
[62] G. Kresse and J. Furthmüller, Comput. Mater. Sci. **6**, 15 (1996).
[63] *CRC Handbook of Chemistry and Physics*, 80th ed., edited by D. R. Lide (CRC Press, Boca Raton, 1999).
[64] J. P. Perdew, J. A. Chevary, S. H. Vosko, K. A. Jackson, M. R. Pederson, D. J. Singh, and C. Fiolhais, Phys. Rev. B **46**, 6671 (1992).
[65] S. H. Vosko, L. Wilk, and M. Nusair, Can. J. Phys. **58**, 1200 (1980).
[66] G. Henkelman, B. P. Uberuaga, and H. A. Jónsson, J. Chem. Phys. **113**, 9901 (2000).
[67] P. Pulay, Chem. Phys. Lett. **73**, 393 (1980).
[68] J. Heyd, G. E. Scuseria, and M. Ernzerhof, J. Chem. Phys. **118**, 8207 (2003).
[69] J. Heyd, G. E. Scuseria, and M. Ernzerhof, J. Chem. Phys. **124**, 219906 (2006).
[70] C. Van de Walle and J. Neugebauer, J. Appl. Phys. **95**, 3851 (2004).
[71] A. H. Castro Neto, F. Guinea, N. M. R. Peres, K. S. Novoselov, and A. K. Geim, Rev. Mod. Phys. **81**, 109 (2009).
[72] J. D. Bernal, Proc. R. Soc. London, Ser. A **106**, 749 (1924).
[73] H. Lipson and A. R. Stokes, Proc. R. Soc. London, Ser. A **181**, 101 (1942).
[74] A. Bosak, M. Krisch, M. Mohr, J. Maultzsch, and C. Thomsen, Phys. Rev. B **75**, 153408 (2007).
[75] R. K. Raman, Y. Murooka, C. Y. Ruan, T. Yang, S. Berber, and D. Tománek, Phys. Rev. Lett. **101**, 077401 (2008).
[76] J. Abrahamson and R. G. A. R. Maclagan, Carbon **22**, 291 (1984).
[77] P. O. Lehtinen, A. S. Foster, A. Ayuela, A. Krasheninnikov, K. Nordlund, and R. M. Nieminen, Phys. Rev. Lett. **91**, 017202 (2003).